Supporting Information for "Rapid cooling and increased storminess triggered by freshwater in the North Atlantic"

M. Oltmanns[1], J. Karstensen[2], G. W. K. Moore[3], S. A. Josey[1]

[1]National Oceanography Centre, Southampton, UK
[2]GEOMAR - Helmholtz Centre for Ocean Research Kiel, Kiel, Germany
[3]University of Toronto, Toronto, Canada

Contents of this file

This Supporting Information has five components: The first describes the involved datasets, the second includes a scale analysis of the surface mass balance in the subpolar region, the third provides details on the significance estimates, the fourth presents composites of large freshwater events and the sensitivities underlying these events, and the fifth shows the hydrographic evolution in the Labrador Sea during the Great Salinity Anomaly and the recent freshening.

1. Data Description
2. Surface Mass Balance
3. Significance Tests
4. Composites and Sensitivity
5. Two Past Freshwater Events

Corresponding author: Marilena Oltmanns, `marilena.oltmanns@noc.ac.uk`

1 Data Description

The hydrographic time series were derived from 3749 Argo float profiles in the central Labrador Sea (Fig. 2a), a region characterised by low spatial variability (Yashayaev & Loder, 2016). To construct continuous time series of temperature and salinity for the period 2002–2018 (Fig. S1a and b), we averaged float profiles within 2-week time intervals, filled the remaining time windows with mooring data (mooring 'K1' from GEOMAR, Fig. 2a), and then applied a 6-week running mean to increase the robustness.

Most time steps of the hydrographic time series are influenced by more than 20 profiles, with some time steps involving over 80 profiles (Fig. S1c and d). To assess the error resulting from reduced sampling sizes we repeated the correlation analyses, omitting time steps with less than 5, 10 and 15 profiles. In each case, we found that the correlation amplitudes were either not appreciably different or slightly increased, suggesting that the obtained correlations are lower bounds.

To examine if sensor drifts influenced the salinity measurements of the Argo floats, we compared the Argo time series with the carefully calibrated mooring data at common time steps below a depth of 700 m, where the water is typically more homogeneous. We identify salinity differences of up to $\sim$0.03 g kg^{-1}, which is plausible considering small spatial variations. Noting that both the temperature and the salinity differences (Fig. S1e and f) are approximately one order of magnitude smaller than the investigated cooling and surface freshening (Fig. S4), we infer that, if drifts were present, they do not significantly affect our conclusions.
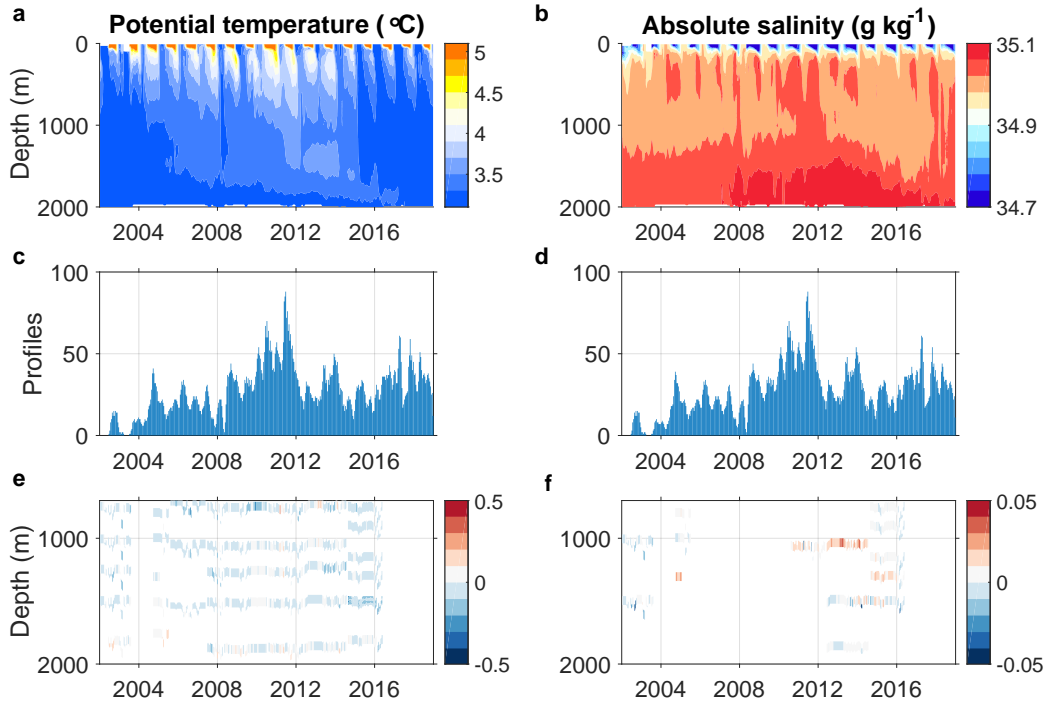

Figure S1. (a,b) Potential temperature and absolute salinity in the Labrador Sea from 2002 to 2018, derived from mooring and Argo float observations. (c,d) Number of Argo profiles included in each time step. (e,f) Differences in the potential temperature and absolute salinity between the mooring and Argo float observations.

This study further took advantage of hydrographic records from the ocean weather station Bravo in the Labrador Sea (Lazier, 1980), mixed layer climatologies derived from Argo floats (Holte et al., 2017), optimal-interpolated, remote sensing-based SST (Reynolds et al., 2002) from the National Oceanic and Atmospheric Administration (NOAA), long-term, in-situ SST (HadISST1) from the Hadley Centre (Kennedy et al., 2011), gridded, altimetrically derived absolute dynamic topography distributed by the Copernicus Marine Environment Monitoring Service (Le Traon et al., 1998) and atmospheric data from the ERA-Interim reanalysis by the European Centre for Medium-Range Weather Forecasts (Dee et al., 2011).

The NAO index was obtained from the NOAA Climate Prediction Center. Following earlier studies (Barnston & Livezey, 1987), it was calculated based on the Rotated Principal Component Analysis applied to the monthly standardized 500-mb geopotential height anomalies between 20N and 90N.

2 Surface Mass Balance

2.1 Estimating the surface freshening

To estimate the surface freshening, we evaluated the mass budget for a shallow surface layer from summer to winter (Griffies & Greatbatch, 2012; Gill, 2016):

$$\int_{-H}^{0} \frac{\partial \rho}{\partial t} \, dz + \nabla \cdot \int_{-H}^{0} \overrightarrow{u} \rho \, dz = -\frac{B}{g} - M, \tag{1}$$

where g is the gravitational acceleration, H is a typical mixed layer depth of 30 m in summer, obtained from Argo float mixed layer depth climatologies in the cooling region (Holte et al., 2017), $\overrightarrow{u}$ is the horizontal velocity, ρ is density, B is the downward buoyancy flux through the surface and M is the downward mass flux through the base of the surface layer. In general, there is an additional term associated with a variable, free surface but on the investigated timescales of months, this term can be neglected because of geostrophic adjustment processes (Griffies & Greatbatch, 2012).

Assuming that the density is constant with depth in the surface layer and defining the depth-averaged velocity $\overrightarrow{u_m}$, the mass budget for an incompressible flow reduces to:

$$-H\rho_{ref}\alpha \left(\frac{\partial}{\partial t} + \overrightarrow{u_m} \cdot \nabla \right) T + H\rho_{ref}\beta \left(\frac{\partial}{\partial t} + \overrightarrow{u_m} \cdot \nabla \right) S = -\frac{B}{g} - M, \tag{2}$$

where we have linearised the equation of state. Here, α and β are the thermal and haline expansion coefficients, T is the temperature, S is the salinity and ρ_{ref} is a reference density of 1025 kg m^{-3}.

Since previous studies found that the NAO in summer is anti-correlated with the melting over Greenland (Hanna et al., 2013) and the Arctic sea ice export (Haine et al., 2015), both potential sources of freshwater, we tested the suitability of the NAO index in summer, multiplied by -1, as a freshwater index (F_{NA}). Thus, we regressed each term of Eq. (2) onto F_{NA} and compared their magnitudes in a scaling analysis.

The first term on the left-hand side represents a widespread, anomalous surface cooling, extending over the full subpolar region (Fig. S2a). With regard to the wide extent of the cooling, exceeding $L \approx 1000$ km, we first compared the local time rate of change with horizontal advection.

The wind-driven Ekman transport, which has the largest contribution to the ageostrophic advection over the central gyre region, has an average speed of less than 10^{-3} m s^{-1}, even if all transport occurs within the shallow layer of 30 m (Fig. S2b). Also, it is not significantly correlated with F_{NA} over the most part of the cooling region and its direction is inconsistent with the distribution of the surface cooling (Fig. S2b).

Estimating a maximum ageostrophic flow of $U \approx 0.01$ m s^{-1}, averaged over the cooling region from summer to winter, the local mass change over the time $\tilde{T} \approx 10^{-7}$ s from summer to winter is at least one order of magnitude larger than that associated with the ageostrophic flow: $\frac{1}{\tilde{T}} \gg \frac{U}{L}$. For a geostrophic flow, the advection term vanishes since there is no geostrophic surface flow across density contours.

Next, we estimated the buoyancy flux anomaly (Cronin & Sprintall, 2009; Gill, 2016), which consists of a heat and a freshwater flux component $B = \frac{g\alpha}{c_p}Q + g\beta S(P - E)$, where c_p is the heat capacity, Q is the heat flux (positive downward) and $P-E$ is the freshwater flux (in kg m^{-2} s^{-1}). To evaluate the buoyancy flux, we obtained the surface heat and freshwater fluxes from ERA-I, estimated α and β from the NOAA SST data and used an average salinity of 34.5 g kg^{-1}, noting that the results do not change appreciably if a salinity of 34.0 g kg^{-1} or 35.0 g kg^{-1} is used instead.

Evaluating the buoyancy flux and regressing it on F_{NA}, we find that it does not match the distribution of the surface cooling (Fig. S2c). Over the southeastern subpo-
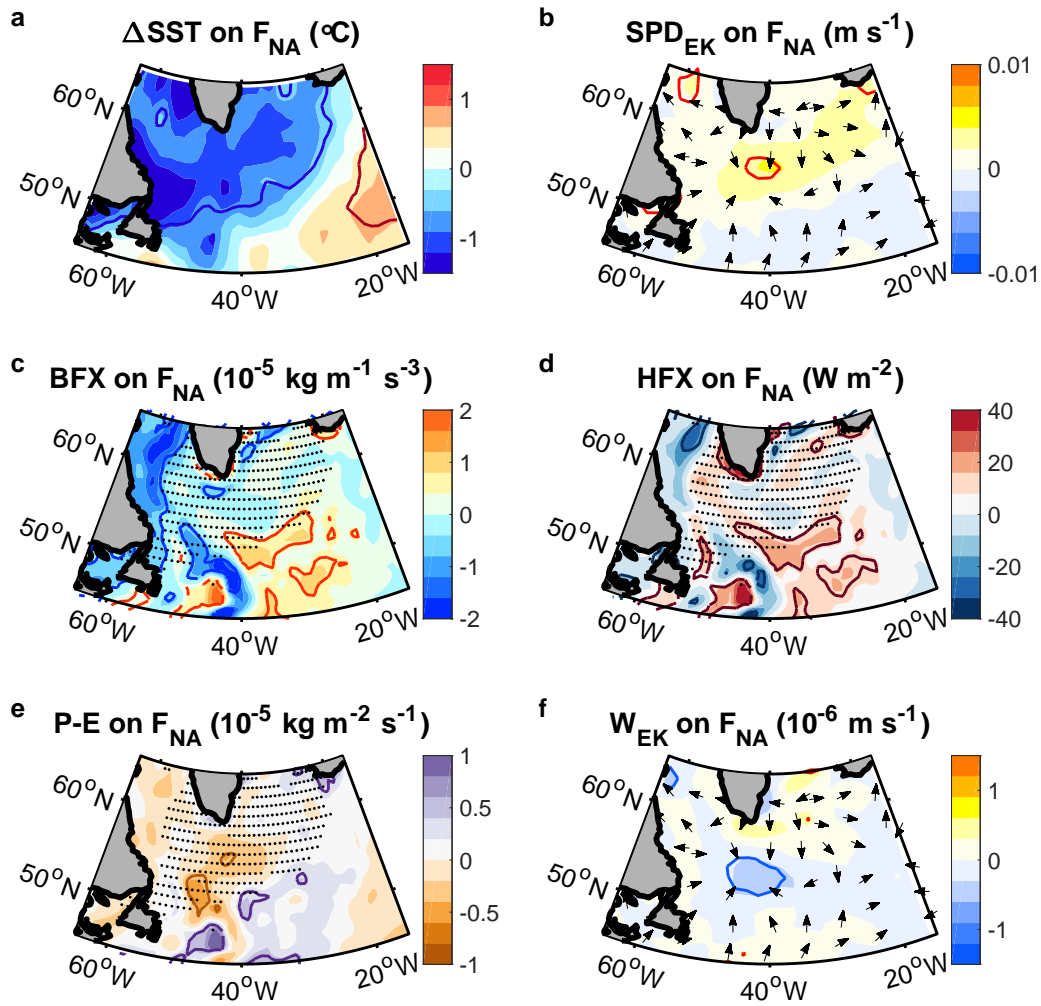
Figure S2. Regressions of (a) the SST change, (b) the speed and direction of the Ekman flow when averaged over the upper 30 m, (c) the buoyancy flux, (d) the heat flux (e) the freshwater flux (precipitation minus evaporation) and (f) the Ekman pumping velocity from August through March onto F_{NA}. All fluxes are positive when they are downward and the Ekman pumping velocity is positive when it is upward. The dots in c, d and e mark the region of the mass balance calculations. Thick contours in all panels show the 95% confidence levels.

lar region, the buoyancy flux anomaly is even increased, implying an enhanced density loss, which stands in contrast to the density gain expected from the cooling. The heat flux anomaly, which accounts for the most part of the the buoyancy flux, is also increased (Fig. S2d). Thus, there is a *reduced* heat loss after high F_{NA} summers, despite the enhanced surface cooling.

When averaged over the interior cooling region and integrated from summer to winter, the buoyancy flux anomaly associated with F_{NA} leads to a mass increase of ~0.09 kg m^{-2}. For the same region and time, and assuming the SST to be representative for the upper 30 m, the widespread cooling signal on the left-hand side of Eq. (2) reflects a mass increase of ~4.7 kg m^{-2}, which is more than one order of magnitude larger even if all temperature changes beneath the surface layer are neglected.

We note that the region northwest of the Labrador Sea has been excluded from the mass balance calculations since it is typically covered by sea ice in winter and we did not include the buoyancy fluxes resulting from the melting and formation of sea ice. Here, we focussed on the cooling in the interior subpolar region (shown in Figure S2) but the obtained ratios do not change appreciably if the surface mass balance is averaged over the full cooling region.

Considering that there is no upwelling due to Ekman suction in the cooling region (Fig. S2f) and that the climatological mean cooling from summer to winter is primarily driven by the surface forcing (Spall & Pickart, 2003; Foukal & Lozier, 2018), the amplitude of M must be less than or equal to that of $\frac{B}{g}$. Thus, both the horizontal and vertical mass fluxes are approximately one order of magnitude smaller than the mass increase associated with the observed, local cooling and the mass balance simplifies to:

$$(-\alpha\Delta T)^* + (\beta\Delta S)^* \approx 0, \tag{3}$$

where the asterisk indicates the regression on F_{NA} and Δ refers to the change from summer to winter.

Eq. (3) states that the density increase associated with the surface cooling is compensated for by a density decrease associated with an enhanced surface freshening. The cooling can thus be understood in terms of a faster adjustment of a fresh surface layer, to the lower air temperature in fall and winter. For Eq. (3) to be valid, the SST does not need to be representative of the temperature in the full surface layer as long as the density is approximately constant and any increase of the temperature anomaly with depth is accompanied by a corresponding increase in the salinity anomaly. We conclude:

$$(\beta\Delta SSS)^* \approx (\alpha\Delta SST)^*. \tag{4}$$

2.2 Estimating the freshwater anomaly

To estimate the freshwater anomaly associated with the cold anomaly in winter, we again compared the magnitude of the terms in the surface mass balance, this time regressed on positive F_{NA} values. Again, we find that the extent of the cold anomaly is too wide for it to be driven by ageostrophic advection (Fig. S3a). In addition, the Ekman transports and Ekman pumping are not significantly correlated with F_{NA} and inconsistent with the distribution of the cold anomaly (Fig. S3b and c).

The surface fluxes cannot account for the cold anomaly either. When averaged over the cold anomaly and integrated over the winter (January through March), the total buoyancy flux leads to an anomalous mass decrease of $\sim$14 kg m^{-2} (Fig. S3d), whereas the cold anomaly reflects an anomalous mass increase of $\sim$-52 kg m^{-2}, assuming an average mixed layer depth H of $\sim$248 m in winter, obtained from Argo climatologies in the cooling region (Holte et al., 2017). Thus, the mass change associated with the surface fluxes is again smaller and also of the opposite sign, implying that

$$(\beta SSS)^* \approx (\alpha SST)^*, \tag{5}$$

yields a lower bound for the freshening associated with the cold anomaly, where the asterisk now indicates the regression on positive F_{NA} values. Again, the obtained ratio does not change appreciably if the full cold anomaly region is considered.
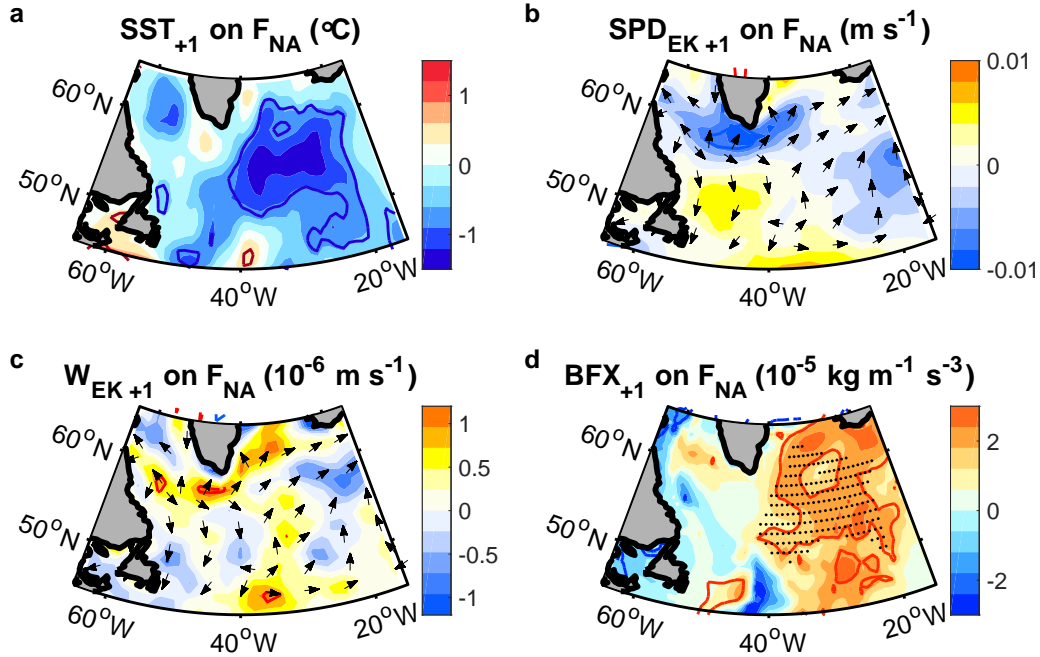

Figure S3. Regression of (a) the SST, (b) the speed and direction of the Ekman flow when averaged over the upper 30 m, (c) the Ekman pumping velocity and (d) the buoyancy flux anomaly in winter (January through March) onto F_{NA} from the preceding summer, including only summers with positive F_{NA}. The buoyancy flux is positive when it is downward and the Ekman pumping velocity is positive when it is upward. The dots in d mark the region of the mass balance calculations. Thick contours in all panels show the 95% confidence levels.

2.3 Comparing the freshwater estimate with observations

According to Eq. (5), the density increase associated with the cold anomaly is compensated for by the density decrease resulting from the additional freshwater. To test the validity of this relationship against observations, we compared the salinity anomaly, inferred from the temperature, with the salinity anomaly, observed by Argo floats, in the fresh winters 2015 and 2016, when F_{NA} was high and we expect the surface temperature to be controlled by the surface freshwater.

Based on the mixed layer properties derived from the Argo floats (Holte et al., 2017), we find that the inferred salinity anomalies are in adequate agreement with the observations, having a root mean square error of $\sim$0.09 g kg^{-1} and a correlation of 0.72. Over the full subpolar region, the estimated values closely follow the best linear fit, supporting the suitability of F_{NA} as an index for freshwater (Fig. S4).
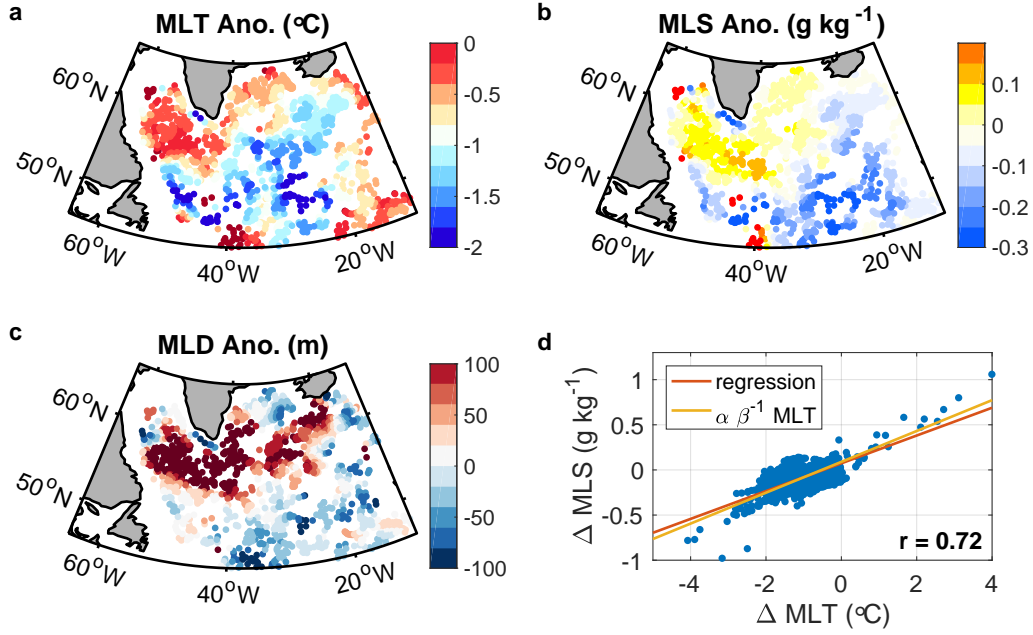

Figure S4. (a,b,c) Mixed layer temperature (MLT), salinity (MLS) and depth (MLD) anomalies from January through April in 2015 and 2016, derived from Argo profiles (Holte et al., 2017). The anomalies are relative to the climatological mean, obtained by from all other profiles in winter (January through April) within 2° longitude and 1° latitude. (d) Comparison of the MLS anomalies, estimated from MLS $\approx \frac{\alpha}{\beta}$ MLT, with a linear regression of the observed MLS anomalies on the MLT anomalies.

3 Significance Tests

Since the correlation analyses were motivated by predetermined hypotheses, we derived the confidence levels from one-sided Student's t-tests. For instance, in Figure 1, we tested the hypothesis that F_{NA} is associated with an increased surface freshening, with the 95% significance contour indicating that there is a 5% chance that the identified relationship was obtained by chance.

To carry out the t-tests, we first estimated the number of degrees of freedom from the autocorrelations of the involved variables (Fig. S5). Apart from the seasonal SSS changes, CAI over the period 1980–2018 and the absolute dynamic topography over the period 1993–2018, all autocorrelations show a rapid drop at a lag of one year, so for these correlations, we assumed $N - 2$ degrees of freedom, where N is the sample size.

Noting that the autocorrelations of CAI and the absolute dynamic topography show a slower decay and that the autocorrelation of the seasonal SSS changes increases again at a lag of two years, we conducted additional significance tests, where we low-pass filtered F_{NA}, the SSS changes, the SLP and the wind stress curl over three winters and assumed $\frac{N}{3} - 2$ degrees of freedom. We find that neither the resulting regressions nor the significance lines are appreciably different in the two versions because the reduced degrees of freedom are compensated for by higher correlations.

Due to the freshening trend, the autocorrelation of the seasonal SSS changes exhibits an even slower decay (Fig. S5c). Still, after low-pass filtering F_{NA} over 5 summers and assuming $\frac{N}{5} - 2$ degrees of freedom, the 95% significance region does not change appreciably and the mean correlation in this region now amounts to $\sim$-0.90 (Fig. S6). For comparison, the autocorrelation of the 5-year low-pass filtered seasonal SSS change is $\sim$0.37 at a lag of 5 years.

For the correlation between F_{NA} and CAI, only positive F_{NA} values were used, so the underlying time series are not continues. To estimate the number of degrees of freedom, we selected the longest continuous time interval of eight years from 2005 to 2012. Over this time, the autocorrelations of CAI and F_{NA} at one year lag are $\sim$0.11 and $\sim$0.34 respectively, whereas the correlation between them is $\sim$0.87. Thus, we assumed $N-2$ degrees of freedom. The different autocorrelations of CAI can be understood by noting that, over the shorter period from 2005 to 2012, the SST was controlled by fluctuations in the surface freshwater, whereas on long periods, it is dominated by low-frequency climate variations (Fig. S5e).

As an additional test, we investigated the strength of the each of the correlations as a function of timescale, using the multi-taper coherence method with adaptive weighting and assuming a stationary bivariate Gaussian distribution of the coherence coefficients to determine the 95% confidence levels (Percival et al., 1993). As expected, we find that most of the correlations are highest on time scales of several years (Fig. S5).
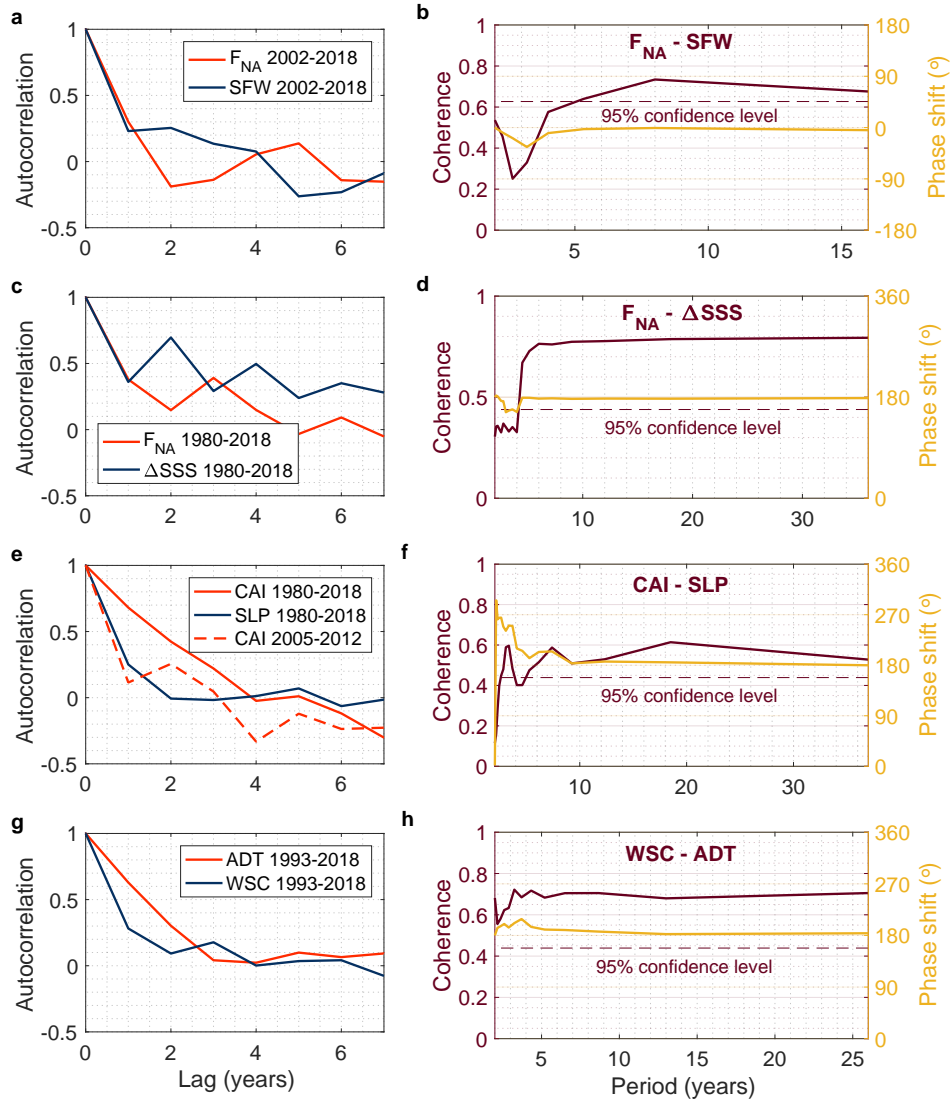
Figure S5. Autocorrelations and coherences for the investigated relationships. SFW refers to the freshwater anomaly in the upper 20 m of the Labrador Sea, averaged from September through February. ADT (WSC) is the absolute dynamic topography (wind stress curl) within the blue (red) contour in Fig. 4e (Fig. 4d), and ΔSSS and the SLP have been averaged over the regions delineated by the blue contours in Fig. 1b and 4a.
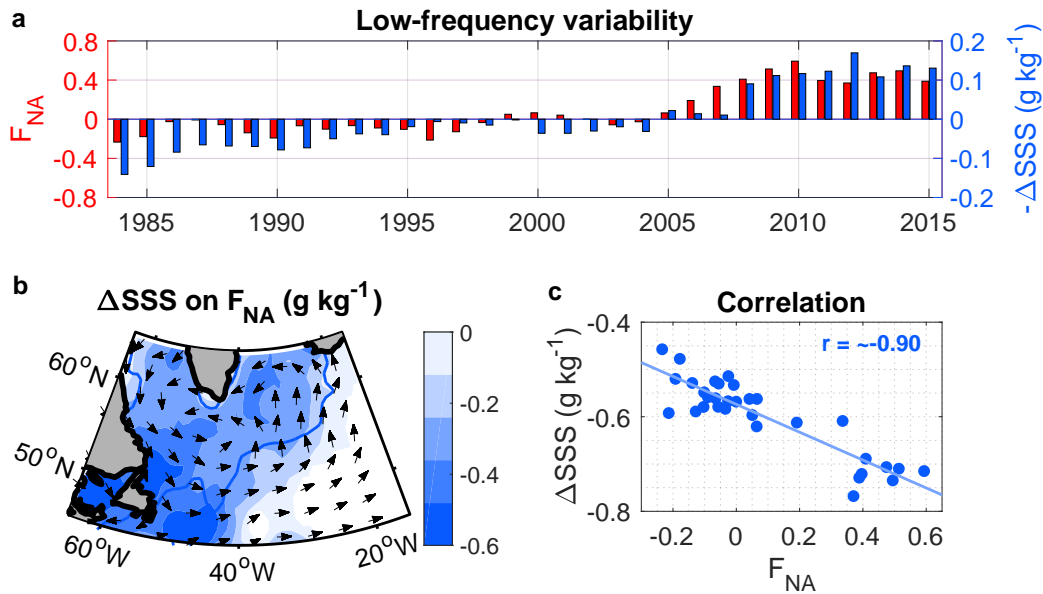
Figure S6. (a) Variability of the low-pass filtered F_{NA} and the inferred surface freshening $(-\Delta SSS)$ in the region enclosed by the blue 95% confidence line in b from summer (August) to winter (January through March). Both F_{NA} and $-\Delta SSS$ have been low-pass filtered over five years. (b) Regression of the inferred SSS change on F_{NA} in the region of the anomalous surface cooling, where again both variables have been low-pass filtered. Thick contours show the 95% confidence level and arrows indicate the direction of the mean geostrophic flow. (c) Correlation between F_{NA} and the seasonal SSS change in the region enclosed by the blue 95% confidence line in b, where again both variables have been low-pass filtered over five years.

4 Composites and Sensitivity

4.1 Composites

Since only positive freshwater anomalies have a decisive influence on the SST and the SST signal in turn needs to be sufficiently strong to also trigger an atmospheric response, we expect the direct relation between freshwater and the atmosphere to be non-linear. Therefore, we first tested this relation with a composite of large freshwater events, which shows that the atmospheric circulation in the winter following the freshwater events is qualitatively similar to that obtained from the regression on the cold anomaly (Fig. S7). The composite also portrays the strengthening of the atmospheric response over the course of the winter and the change in the sign of the surface fluxes from being positive in January and February to negative in March (Fig. S8).
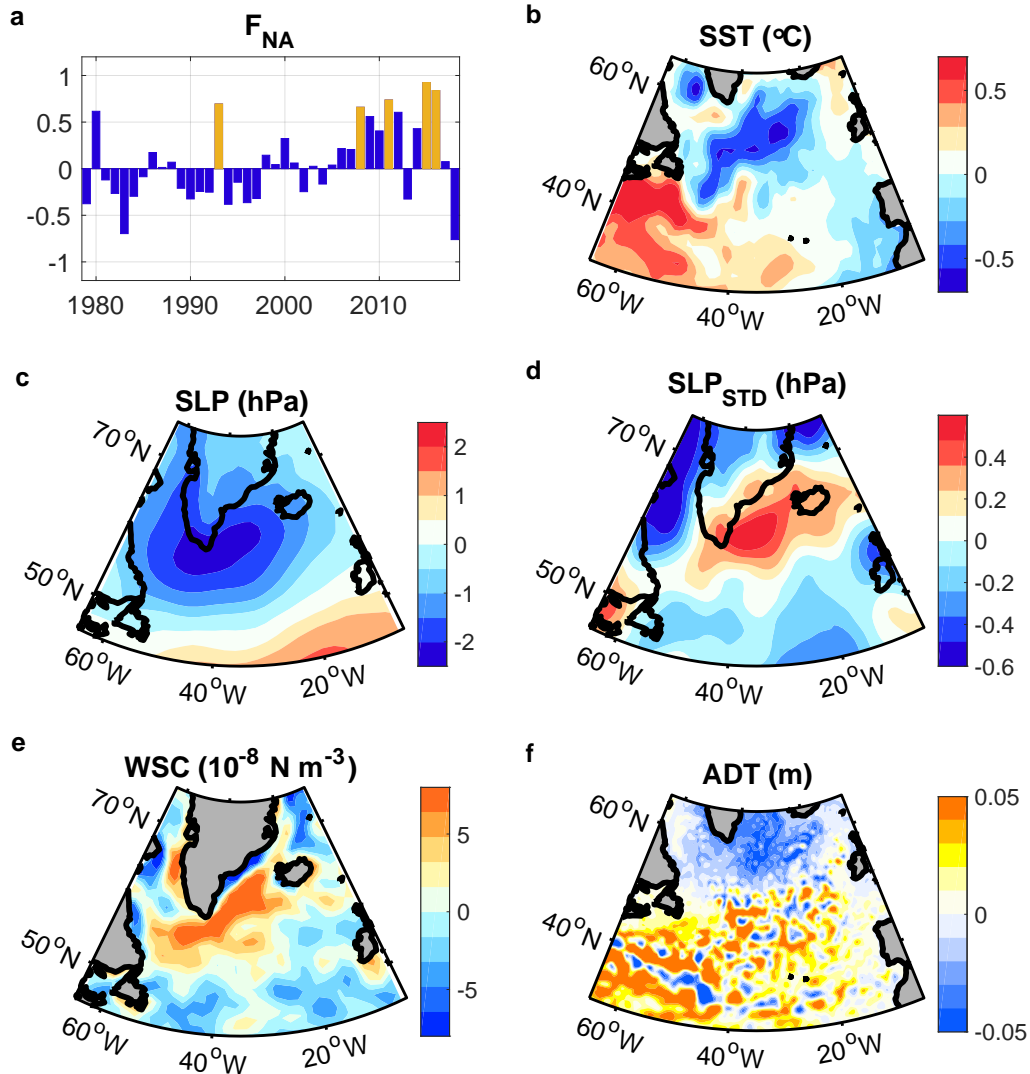

Figure S7. (a) Time series F_{NA} with the yellow years indicating the years used for the composites. (b-f) Composites of (b) the SST, (c) the SLP, (d) the 2 to 6-day band-pass filtered standard deviation of the SLP, (e) the wind stress curl and (f) the absolute dynamic topography in the winters (January through March) after the F_{NA} summers marked in a. For the SST and the dynamic topography, the 1980 event is missing since the data only start in 1982 and 1993.
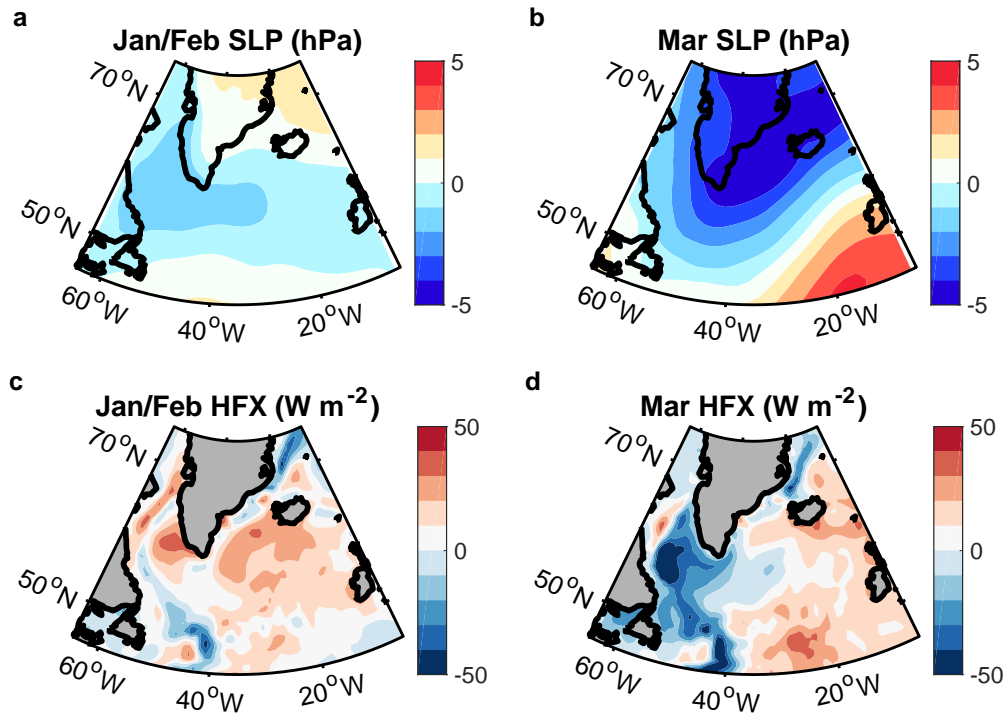
Figure S8. Composites of (a,b) the SLP and (c,d) the surface heat flux in (a,c) January and February (averaged) and (b,d) March in the winter after the F_{NA} summers marked in Fig. S7a. A positive heat flux anomaly means that the ocean loses less heat.

4.2 Sensitivity

When only these large freshwater events are considered, the relationship between F_{NA} and the SST is nearly linear (Fig. 3c). Thus, we next regressed the SST on F_{NA} directly, including only large freshwater events. The obtained direct regressions are again qualitatively similar to the regressions of the atmosphere on CAI (Fig. S9). In addition, their amplitudes are very large, revealing a high sensitivity to small variations in the freshwater when the freshwater concentration is already high.

The high sensitivity can be understood by picturing the one-dimensional mixed layer model $\Delta SST \approx \frac{Q \cdot \Delta t}{c_p \cdot \rho \cdot h}$ where Q is the average surface heat flux over the time interval Δt, ρ is the density, c_p the heat capacity and h the mixed layer depth. By strengthening the stratification, an increased surface freshening decreases the mixed layer depth. Since ΔSST is proportional to $\frac{1}{h}$, a curve that has a very steep slope when h is small, ΔSST is very sensitive to small variations in h and in turn the freshening.
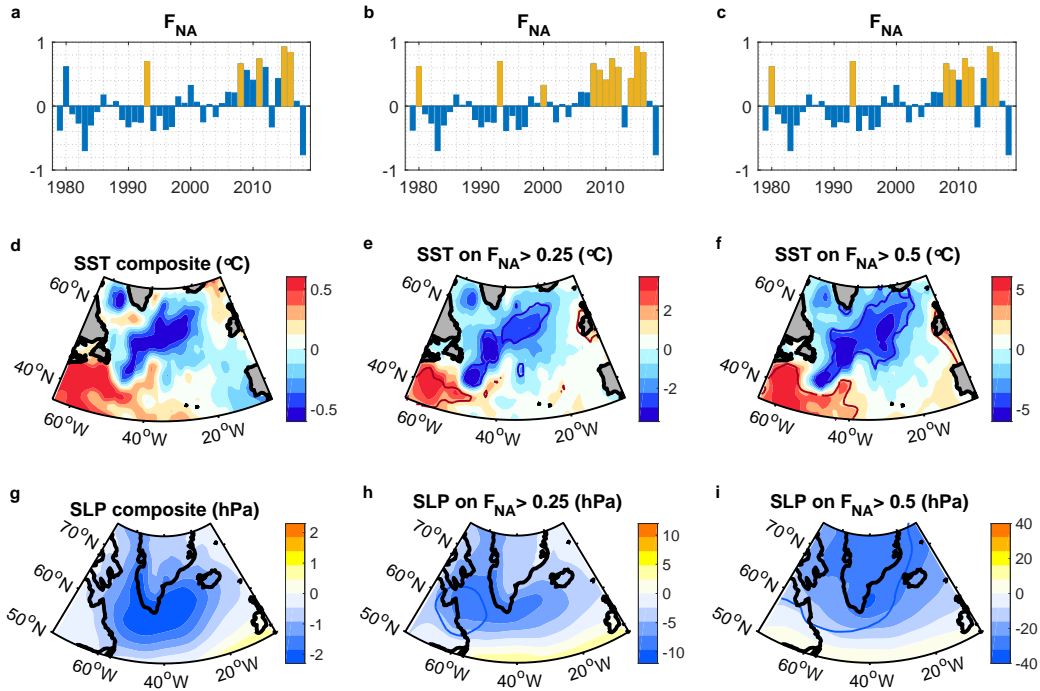

Figure S9. (a,b,c) Time series of F_{NA} with the yellow years indicating the years used for the composites and regressions beneath. (d,g) Composites of the SST and SLP in the winter following the five largest freshwater events. (e,f,h,i) Regressions of the SST and SLP in winter on the F_{NA} from the preceding summer. In e and h, we excluded all summers with F_{NA} values less than 0.25, and in f and i we excluded the years with F_{NA} values less than 0.5. Please note the different colour scales.

The underlying nonlinearity in the relationship between the F_{NA} and the SST (Fig. 3c) stresses the importance of using only high F_{NA} values for the direct regressions of the atmosphere on F_{NA}. However, considering that the observational record is still comparatively short with regard to the occurrence of large freshwater events, the number of degrees of freedom is only low and the significances follow from high correlations. To obtain a higher number of degrees of freedom, we showed the dynamical linkages in the cooling mechanism individually (Figs. 2-4).

4.3 Detrended time series

Since the freshening itself has a trend, the trends represent an important part of the signal that we are investigating, so we did not subtract any trends from the time series. However, the influences of large freshwater events do not change appreciably after subtracting a trend from F_{NA}, the SST and the absolute dynamic topography, and the correlations remain significant (Fig. S10). The atmospheric variables in winter do not have a significant trend over the investigated period.
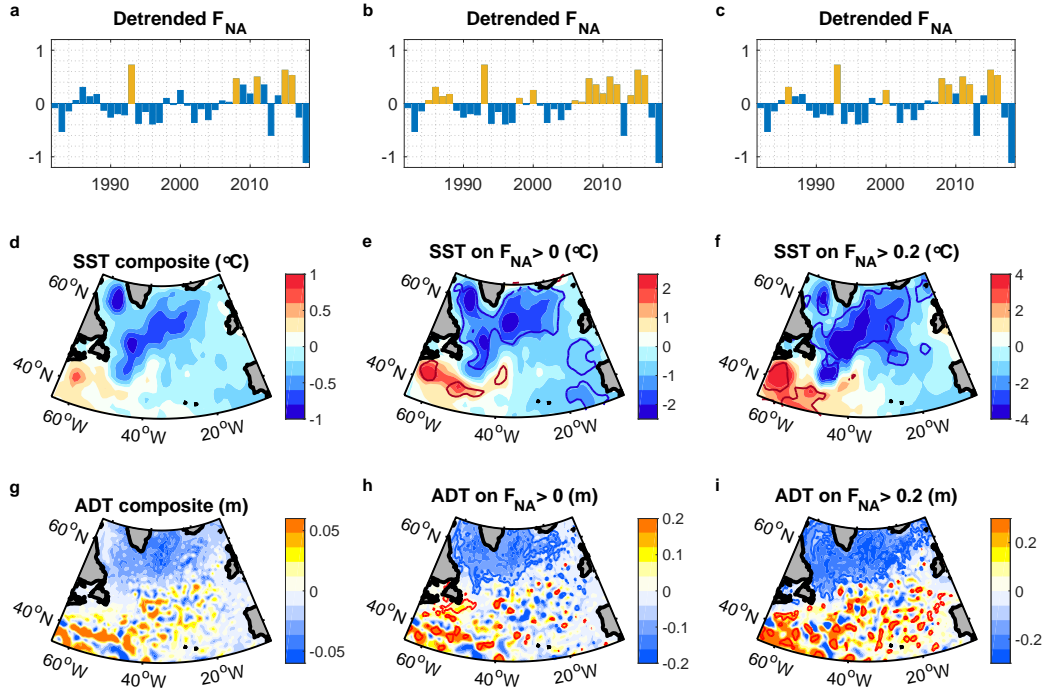

Figure S10. (a,b,c) Time series of the detrended F_{NA} with the yellow years indicating the years used for the composites and regressions beneath. (d,g) Composites of the SST and absolute dynamic topography (ADT) in the winter following the five largest freshwater events. (e,f,h,i) Regressions of the SST and ADT in winter on the F_{NA} from the preceding summer, where F_{NA}, the SST and the ADT have been detrended. In e and h, we excluded all summers with F_{NA} values less than 0, and in f and i we excluded the years with F_{NA} values less than 0.2. Please note the different colour scales.

5 Two Past Freshwater Events

Two freshwater anomalies, particularly well documented in the observational record, are the Great Salinity Anomaly from 1969 to 1972 (Lazier, 1980) and the recent freshening (Holliday et al., 2020), starting around 2008 (Fig. 1a). During the Great Salinity Anomaly, the freshwater remained at the surface throughout the three-year period, while the recent freshening was characterised by repeatedly high F_{NA} values, with peaks between 2008 and 2012 and in 2015/2016, coincident with high freshwater anomalies in the Labrador Sea (Fig. S11a and b).
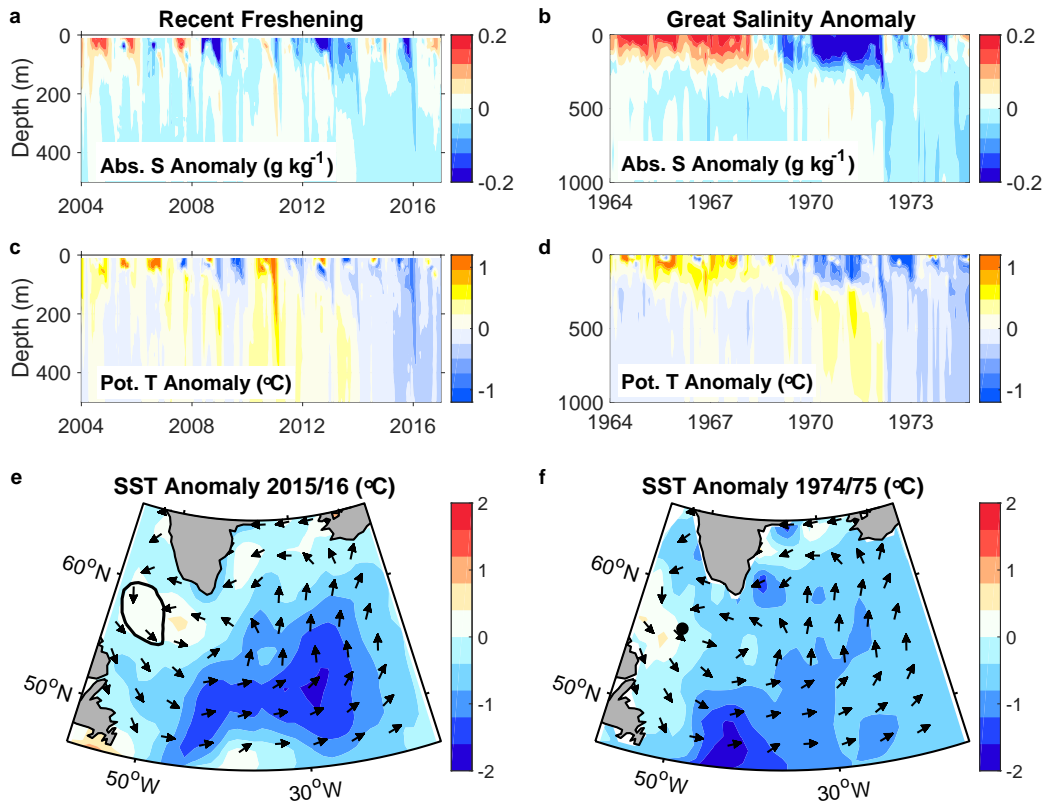

Figure S11. (a–d) Absolute salinity and potential temperature anomalies in the Labrador Sea during the recent freshening, observed by Argo floats, and during the Great Salinity Anomaly, observed by the ocean weather station Bravo. All anomalies are with respect to the mean annual cycle. (e,f) SST anomaly from January through April in (e) 2015/2016, based on the NOAA SST data, and in (f) 1974/1975, based on the Hadley Centre SST data. The black contour in e delineates the Argo float sampling region, the black circle in f marks the location of the weather station Bravo and the arrows in e and f indicate the direction of the mean geostrophic flow.

Both the Great Salinity Anomaly and the individual peaks in the recent freshwater event started with a freshening and cooling at the surface and were followed by a deeper cooling that reached depths below 1000 m in the Labrador Sea (Fig. S11a–d). During the mixed layer deepening, the temperature and salinity anomalies decreased while being distributed over a larger depth range. Thus, the strongest SST anomalies appeared outside the deep convection region in the Labrador Sea and amounted to ∼-1.5 °C after the Great Salinity Anomaly and ∼-2 °C after the recent freshening (Fig. S11e and f).

References

Barnston, A. G., & Livezey, R. E. (1987). Classification, seasonality and persistence of low-frequency atmospheric circulation patterns. *Monthly weather review*, *115*(6), 1083–1126.

Cronin, M., & Sprintall, J. (2009). Wind-and buoyancy-forced upper ocean. *Elements of Physical Oceanography: A derivative of the Encyclopedia of Ocean Sciences*, 237–245.

Dee, D. P., Uppala, S., Simmons, A., Berrisford, P., Poli, P., Kobayashi, S., . . . others (2011). The era-interim reanalysis: Configuration and performance of the data assimilation system. *Quarterly Journal of the royal meteorological society*, *137*(656), 553–597.

Foukal, N. P., & Lozier, M. S. (2018). Examining the origins of ocean heat content variability in the eastern north atlantic subpolar gyre. *Geophysical Research Letters*, *45*(20), 11–275.

Gill, A. E. (2016). *Atmosphere—ocean dynamics.* Elsevier.

Griffies, S. M., & Greatbatch, R. J. (2012). Physical processes that impact the evolution of global mean sea level in ocean climate models. *Ocean Modelling*, *51*, 37–72.

Haine, T. W., Curry, B., Gerdes, R., Hansen, E., Karcher, M., Lee, C., . . . others (2015). Arctic freshwater export: Status, mechanisms, and prospects. *Global and Planetary Change*, *125*, 13–35.

Hanna, E., Jones, J. M., Cappelen, J., Mernild, S. H., Wood, L., Steffen, K., & Huybrechts, P. (2013). The influence of north atlantic atmospheric and oceanic forcing effects on 1900–2010 greenland summer climate and ice melt/runoff. *International Journal of Climatology*, *33*(4), 862–880.

Holliday, N. P., Bersch, M., Berx, B., Chafik, L., Cunningham, S., Florindo-López, C., . . . others (2020). Ocean circulation causes the largest freshening event for 120 years in eastern subpolar north atlantic. *Nature Communications*, *11*(1), 1–15.

Holte, J., Talley, L. D., Gilson, J., & Roemmich, D. (2017). An argo mixed layer climatology and database. *Geophysical Research Letters*, *44*(11), 5618–5626.

Kennedy, J., Rayner, N., Smith, R., Parker, D., & Saunby, M. (2011). Reassessing biases and other uncertainties in sea surface temperature observations measured in situ since 1850: 1. measurement and sampling uncertainties. *Journal of Geophysical Research: Atmospheres*, *116*(D14).

Lazier, J. R. (1980). Oceanographic conditions at ocean weather ship bravo, 1964–1974. *Atmosphere-ocean*, *18*(3), 227–238.

Le Traon, P., Nadal, F., & Ducet, N. (1998). An improved mapping method of multisatellite altimeter data. *Journal of atmospheric and oceanic technology*, *15*(2), 522–534.

Percival, D. B., Walden, A. T., et al. (1993). *Spectral analysis for physical applications.* cambridge university press.

Reynolds, R. W., Rayner, N. A., Smith, T. M., Stokes, D. C., & Wang, W. (2002). An improved in situ and satellite sst analysis for climate. *Journal of climate*, *15*(13), 1609–1625.

Spall, M. A., & Pickart, R. S. (2003). Wind-driven recirculations and exchange in the labrador and irminger seas. *Journal of Physical Oceanography*, *33*(8), 1829–1845.

Yashayaev, I., & Loder, J. W. (2016). Recurrent replenishment of labrador sea water and associated decadal-scale variability. *Journal of Geophysical Research: Oceans*, *121*(11), 8095–8114.